RSC Advances

PAPER

View Article Online
View Journal | View Issue

Cite this: *RSC Adv.*, 2018, **8**, 40676

Electrical conductivity and vibrational studies induced phase transitions in $[(C_2H_5)_4N]FeCl_4$

Kh. Ben Brahim, M. Ben gzaiel, A. Oueslati * and M. Gargouri

The compound, tetraethylammonium tetrachloroferrate $[(C_2H_5)_4N]FeCl_4$, was prepared by slow evaporation at room temperature. It was characterized by X-ray powder diffraction, thermal analysis, and impedance and vibrational spectroscopy. X-ray diffraction data confirmed formation of a single phase material which crystallized at room temperature in the hexagonal system ($P6_3mc$ space group). DSC showed the existence of two phase transitions at 413 K and 430 K. Electrical conductivity was measured in the temperature and frequency ranges of 390 K to 440 K and 40 Hz to 110 MHz, respectively. Nyquist plots revealed the existence of grains and grain boundaries that were fitted to an equivalent circuit. AC conductivity plots were analyzed by Jonscher's power law. Variations in the "*s*" values indicated that CBH models describe the conduction mechanism in regions I and II. Temperature dependence of Raman spectra showed that the most important changes were observed in the cationic parts ($[(C_2H_5)_4N]^+$). The activation energy value obtained from the line width decreased which indicated an order–disorder model.

Received 14th September 2018
Accepted 25th November 2018

DOI: 10.1039/c8ra07671e

rsc.li/rsc-advances

1. Introduction

Recently, material science has mainly concentrated on multifunctional materials. Obtaining such a material in the form of solids with a continuous lattice was found to be very complicated. However, a material with a multifunctional character can be obtained by building up hybrid solids formed by two lattices consisting of organic and inorganic parts. Much attention has been paid to organic–inorganic hybrid materials due to the possibility of each moiety contributing its own characteristic properties.[1–5] This large family exhibits several phase transitions related to the reorientation dynamic of alkyl chains.[6–8] In fact, they present interesting properties such as ferromagnetic, ferroelectric, ferroelastic, and thermal ones.[9–13]

Special attention is paid to compounds based on iron. Owing to the presence of the high-spin d^5 in their molecules. Compounds containing tetrahalogenferrate(III) units may also be used as attractive magnetic materials.[14,15] Moreover, it was found that some of the iron(III) complexes have been used in bioinorganic chemistry as substances for synthesizing model compounds, such as $[Fe_2S_2Cl_4]^{2-}$.[16]

With this aim, we wish to report the growth of $[(C_2H_5)_4N]FeC1_4$ crystals, and a description of basic information about their properties. This compound is of interest due to the presence of Fe(III) in a tetrahedral coordination structure that mainly provides the existence of magnetic, electric, and elastic anomalies.[17] At room temperature, the system belongs to the hexagonal system (space group $P6_3mc$) with four formulae per unit cell, which has dimensions of $a = b = 8.198$ Å, $c = 13.183$ Å.[18]

In this contribution, the synthesis, X-ray powder diffraction, differential scanning calorimetry, impedance measurements, and vibrational study as a function of temperature were carried out.

2. Experimental details

2.1 Synthesis

Mixing a stoichiometric molar ratio of $FeCl_3$ (purity 98%; FLUKA) and $[N(C_2H_5)_4]Cl$ (purity 97%; FLUKA) was performed in aqueous solution. After few days, yellow prismatic crystals were obtained by slow evaporation at room temperature. The sequence of the chemical reaction is the following:

$$[(C_2H_5)_4N]Cl + FeCl_3 \rightarrow [(C_2H_5)_4N]FeCl_4$$

2.2 Characterisations

Phase purity and homogeneity were checked using X-ray powder diffraction analysis. Using a Phillips PW 1710 powder diffractometer operating with CuK_α ($\lambda = 1.5405$ Å), the XRD pattern was recorded in a wide range of Bragg angles ($10° \leq 2\theta \leq 60°$). Structural refinements ware carried out by the Rietveld refinement method.[19] Differential scanning calorimetry, DSC, was executed with a Perkin Elmer DSC-7 instrument in a temperature range from 300 K to 470 K with a 5 K min^{-1} rate. Thermogravimetric analysis (TGA) was performed with an ATG-Q500 SETARAM in a heating process from room temperature up to 772 K with a heating rate of 10 K min^{-1}.

Laboratory for Spectroscopic Characterization and Optics of Materials, Faculty of Sciences, University of Sfax, B. P. 1171, 3000 Sfax, Tunisia. E-mail: oueslatiabderrazek@yahoo.fr

To study the electrical proprieties, the $[(C_2H_5)_4N]FeCl_4$ powder was pressed at 5 t cm^{-2} ton pressure, forming a circular disc with a 1.1 mm thickness and 8 mm diameter. Measurements were executed in the frequency range of 40 Hz to 110 MHz using a 4294A impedance analyzer. The measurements were carried out under an excitation voltage of 50 mV. In the present study, we found that after several tests our pellet became softer after 430 K, which proved that these organic–inorganic crystals of tetraethylammonium tetrachloroferrate show plastic behavior at high temperature.[6] Therefore, the sample is not in the form of an electrical dipole, which shows that measurement after 430 K is not possible.

Using a Perkin Elmer FT-IR 1000 spectrophotometer, the infrared spectrum of $[(C_2H_5)_4N]FeCl_4$ was recorded at room temperature in the frequency range of 500–3500 cm^{-1}.

Raman scattering measurements were analyzed by a Horibe Jobin-Yvon T64000 spectrometer over the frequency range 50–3500 cm^{-1} with a resolution of 3 cm^{-1} in the temperature range 303–428 K. The program LABSPEC5 software was used for fitting the spectra with a combination of Lorentzian–Gaussian functions. The fitting procedure was performed in order to quantitatively analyze the evolution of Raman bands as a function of temperature.

3. Results and discussion

3.1 X-ray powder diffraction analysis

Fig. 1 shows the XRD patterns of $[(C_2H_5)_4N]FeCl_4$. The Rietveld refinement was performed using the FULLPROOF software program. The circles symbolize the experimental data and the line presents the simulated pattern. The purity of the studied compound was proved and the reflection peaks were indexed in the hexagonal system with the $P6_3mc$ space group. The corresponding lattice parameters were found to be: $a = b = 8.218$ Å, $c = 13.203$ Å and the cell volume was $V = 772.2$ Å^3. The quality of the refinement was evaluated through the goodness of fit where $\chi^2 = 1.23$. The values of the reliability factors obtained from the refinement are $R_{\omega p} = 13.5$, $R_p = 18.5$ and $R_{exp} = 12.04$ and the fitted parameters were found to be in a good agreement with those in the literature.[18]

3.2 Thermal analysis

Fig. 2 shows the DSC thermogram for $[(C_2H_5)_4N]FeCl_4$. The DSC curve was recorded with a heating scan at 5 K min^{-1}. The calorimetric measurement showed that the compound under investigation undergoes discontinuation of two phase

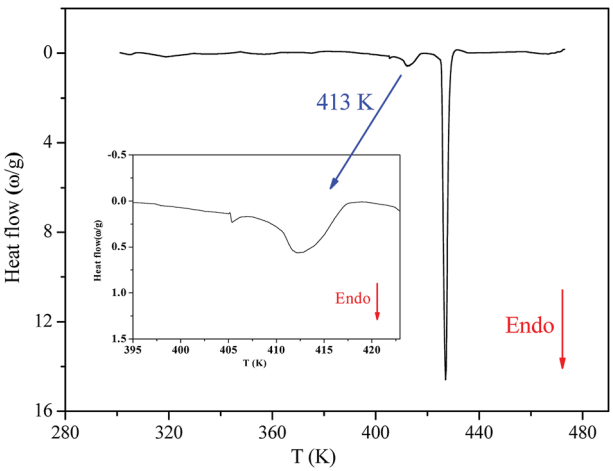

Fig. 2 Differential scattering calorimetric trace of $[(C_2H_5)_4N]FeCl_4$.

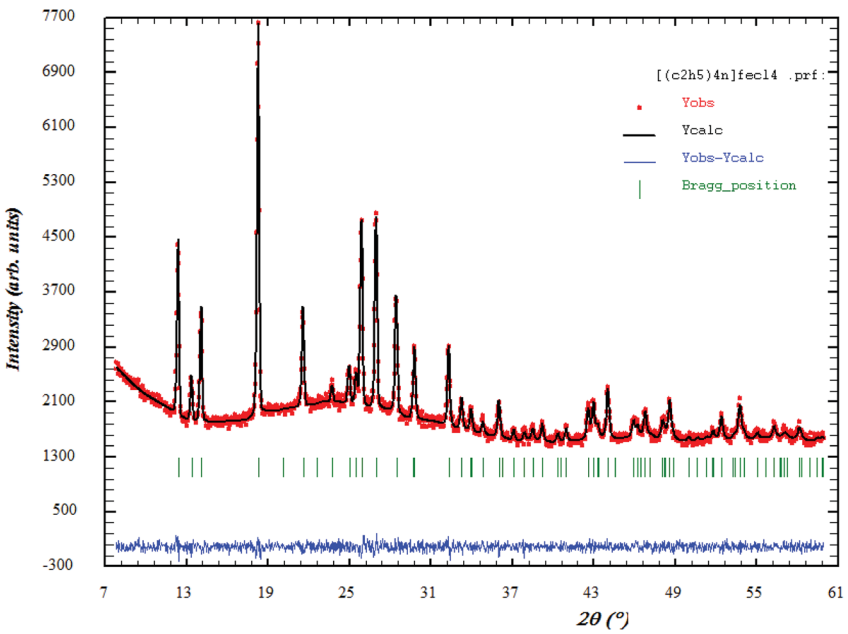

Fig. 1 X-ray diffractogram of $[(C_2H_5)_4N]FeCl_4$ in the 2θ range 10–60°. The red circle indicates the experimental data and calculated data are represented by black continuous lines. The lowest curve in blue shows the difference between experimental and calculated patterns. The green vertical bars describe the Bragg position.

Table 1 The characteristic dynamical values of $[N(C_2H_5)_4]FeCl_4$

T (K)	ΔH J mol^{-1}	ΔS J mol^{-1} K^{-1}
413	459	1.112
430	545	1.267

transitions at $T_1 = 413$ K and $T_2 = 430$ K. The characteristic dynamical values of these phase transitions are listed in Table 1.

From the Boltzmann equation, $(\Delta S = R \ln(\Omega))$, where Ω is the rapport number of distinguishable orientations allowed in the high- and the low temperature phases (N_1/N_2).

The obtained values of Ω were 1.14 and 1.16 at T_1 and T_2, respectively $(\Omega_{1,2} < 2)$, which reveals that these two phase transitions are not purely "order–disorder".[20]

The thermogravimetric analysis (TGA) curve in Fig. 3 shows that this compound started to decompose at 615 K. Besides, no weight losses were observed between 300 and 615 K.

3.3 Electrical measurements

Impedance spectroscopy is one of the most suitable techniques to investigate electrical conductivity and to analyze the charge transport processes in grains, grain boundaries, and electrode effects in materials in terms of thermal and frequency ranges.[21]

Fig. 4 displays the obtained Nyquist plots from experimental results at several temperatures. With respect to these curves, the experimental points show semi-circles where their diameters decrease with temperature increase indicating that the conduction mechanism is thermally activated.[22] In addition, they are centered below the abscissa axis indicting that the relaxation process in the material is of a non-Debye type.[23] (The Debye model presents the ideal response[24] where all the dipoles participating in the relaxation phenomenon have the same relaxation time τ). The Nyquist diagram is a perfect semicircle centered on the abscissa axis but there are other cases where all dipoles do not have the same relaxation time (distribution of relaxation time). There are several empirical models derived from the Debye equation that correctly describe these types of relaxations including the Cole–Cole model[25–27] and the Nyquist plot described by a flattened arc with its center located below the real axis on a line deviated from the angle of $(1 - \alpha)\pi/2$ where α describes the interactions between dipoles.

Nyquist plots were analyzed using Zview Software. The best fits were obtained using an equivalent circuit (inset Fig. 4) realized by two cells which consisted of a parallel combination of bulk resistance R_1 and fractal capacity CPE_1 in series with a parallel combination of grain boundary resistance R_2 and fractal capacity CPE_2. The constant phase element (CPE) impedance is given by the following equation:[28]

$$Z_{CPE} = \frac{1}{Q(j\omega)^{\alpha}} \quad (1)$$

where Q presents the capacitance value of the CPE fractal capacity and α relates to the deviation degree with respect to the pure capacitor value.

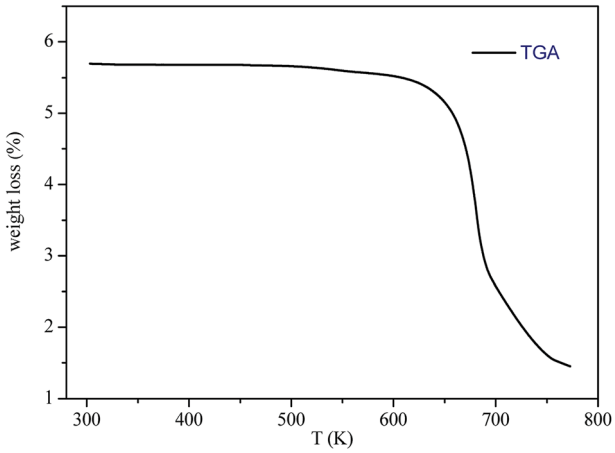

Fig. 3 TGA curve of $[(C_2H_5)_4N]FeCl_4$.

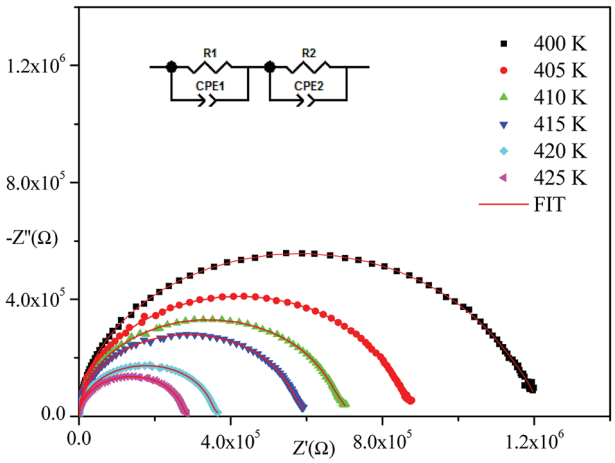

Fig. 4 Complex impedance spectra of $[(C_2H_5)_4N]FeCl_4$ at different temperatures.

The theoretical impedance of real (Z') and imaginary $(-Z'')$ parts linked to the equivalent circuit were calculated according to the following eqn (2) and (3):

$$Z' = \frac{R_1 + R_1^2 Q_1 \omega^{\alpha_1} \cos\left(\alpha_1 \frac{\pi}{2}\right)}{\left[R_1 + R_1^2 Q_1 \omega^{\alpha_1} \cos\left(\alpha_1 \frac{\pi}{2}\right)\right]^2 + \left[R_1 + R_1^2 Q_1 \omega^{\alpha_1} \sin\left(\alpha_1 \frac{\pi}{2}\right)\right]^2} + \frac{R_2 + R_2^2 Q_2 \omega^{\alpha_2} \cos\left(\alpha_2 \frac{\pi}{2}\right)}{\left[R_2 + R_2^2 Q_2 \omega^{\alpha_2} \cos\left(\alpha_2 \frac{\pi}{2}\right)\right]^2 + \left[R_2 + R_2^2 Q_2 \omega^{\alpha_2} \sin\left(\alpha_2 \frac{\pi}{2}\right)\right]^2} \quad (2)$$

$$-Z'' = \frac{R_1^2 Q_1 \omega^{\alpha_1} \sin\left(\alpha_1 \frac{\pi}{2}\right)}{\left[R_1 + R_1^2 Q_1 \omega^{\alpha_1} \cos\left(\alpha_1 \frac{\pi}{2}\right)\right]^2 + \left[R_1 + R_1^2 Q_1 \omega^{\alpha_1} \sin\left(\alpha_1 \frac{\pi}{2}\right)\right]^2} + \frac{R_2^2 Q_2 \omega^{\alpha_2} \sin\left(\alpha_2 \frac{\pi}{2}\right)}{\left[R_2 + R_2^2 Q_2 \omega^{\alpha_2} \cos\left(\alpha_2 \frac{\pi}{2}\right)\right]^2 + \left[R_2 + R_2^2 Q_2 \omega^{\alpha_2} \sin\left(\alpha_2 \frac{\pi}{2}\right)\right]^2} \quad (3)$$

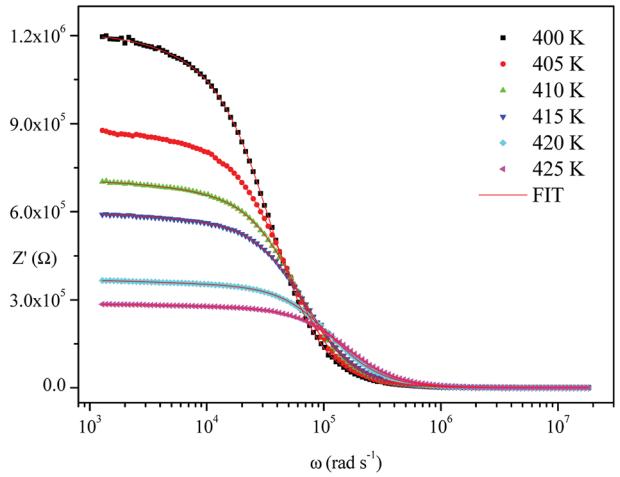

Fig. 5 Variation of the real part of impedance as a function of frequency and temperature.

The frequency dependence of the impedance of real (Z') and imaginary ($-Z''$) at various temperatures, are depicted in Fig. 5 and 6, respectively. It was noted that the magnitude of Z' decreased, where increases in both frequency and temperature indicated an increase in AC conductivity of the sample. At frequencies higher than 10^6 Hz, the coincidence of the impedance (Z') at all temperatures showed a possible freeing of space charge[29] whereas, the Z'' peak maximum decreased with a rise in temperature. The peak frequency ω_{max} shifted to higher values and the later reflected a non-Debye type relaxation.[30]

Fig. 4–6 show good conformity between experimental data and the theoretical line indicating that the equivalent circuit described the electric properties of the investigated compound quite well. As a matter of fact, details of fitted values for different temperatures are gathered in Table 2. It is obvious that all the capacitance values (Q_1 and Q_2) are in the range of picofarads (pF) and nanofarads (nF), respectively, implying a single semicircle response is from grain interiors and grain

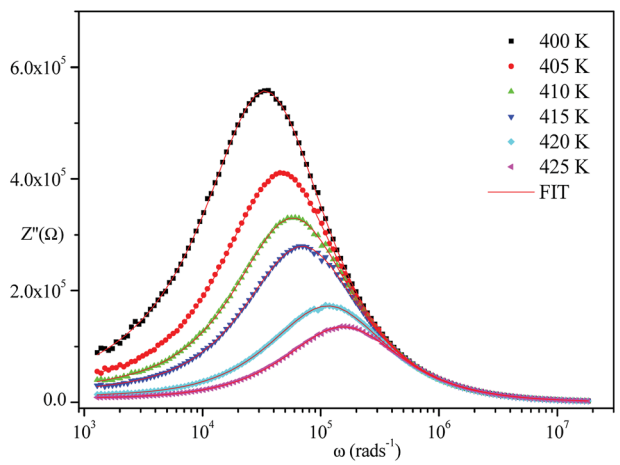

Fig. 6 Variation of the imaginary part of impedance as a function of frequency at various temperatures.

Table 2 Fitted circuit parameters at different temperature

T (K)	R_1 ($\times 10^5$)	Q_1 ($\times 10^{-11}$)	α_1	R_2 ($\times 10^4$)	Q_2 ($\times 10^{-9}$)	α_2
400	10.86	2.856	0.989	12.786	1.943	0.958
405	8.159	2.716	0.993	7.169	6.244	0.916
410	6.597	2.677	0.994	5.358	9.588	0.900
415	5.611	2.654	0.994	4.119	16.94	0.882
420	3.484	2.572	0.996	2.349	41.18	0.833
425	2.726	2.406	0.971	1.562	61.70	0.810

boundaries. The values of α vary in the range of 0.81–0.99 showing a capacitive behavior of the fractal phase CPE.[31]

Electrical conductivity spectroscopy is a well-founded method for characterizing hopping dynamics of the charge carriers. Based on the equivalent circuit parameters, grain conductivity is expressed according to the following expression:[29]

$$\sigma_g = \frac{e}{R_1 S} \quad (4)$$

where e and S are the thickness and area of the sample, respectively, and R_1 is the bulk resistance. The dependence of $\ln(\sigma_g T)$ *versus* $1000/T$ is presented in Fig. 7. The experimental data evinced a linear variation whose σ_g decreased as temperature decreased. This indicated that electrical conduction in the material is a thermally activated process and was fitted well by the Arrhenius relation as described by eqn (5):

$$\sigma_g = \sigma_0 \exp\left(-\frac{E_a}{k_B T}\right) \quad (5)$$

where σ_0 is the pre-exponential factor, E_a is the activation energy, and k_B is the Boltzmann constant.

The activation energies obtained by the linear fit at T_1 (413 ± 5 K) are E_a (I) = 0.74 eV in region I and E_a (II) = 1.13 eV in region II. The observed variation in the activation energies between the two temperature domains can be explained by movement of the cationic and anionic parts with temperature.[32] However, the discontinuity at 413 ± 5 K agrees with the phase transition observed in the DSC measurements.

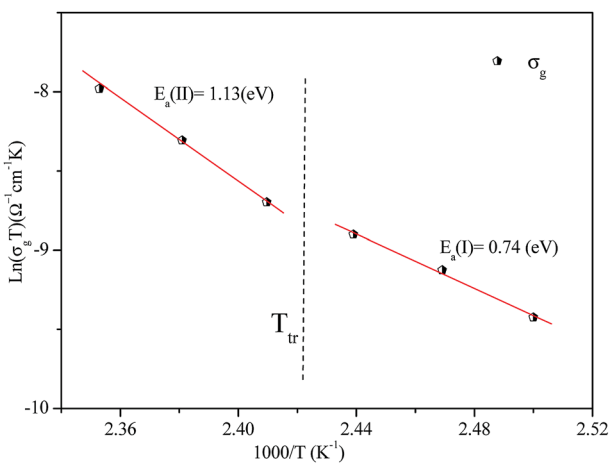

Fig. 7 Plot of $\ln(\sigma_g T)$ *versus* $1000/T$ for the $[(C_2H_5)_4N]FeCl_4$ crystal.

3.4 AC conductivity studies

The variation of AC conductivity with angular frequency for $[(C_2H_5)_4N]FeCl_4$ is shown in Fig. 8 at different temperatures. Each conductivity plot exhibits two distinct regions. First, it remained almost constant at lower frequencies; this plateau corresponds to dc conductivity. It is seen that an increase of temperature is closely related to an increase of the AC conductivity which suggests that electrical conduction in the material is a thermally activated process and suggests semiconductor properties of this compound. Second, at higher frequencies, the AC conductivity dependence occurred with changes in slope and increased gradually with an increase in frequency.

Besides, the dispersive region shifted to higher frequencies with an increase in temperature. This phenomenon of conductivity dispersion is generally analyzed using Jonscher's universal power law[33] expressed by eqn (6):

$$\sigma_{ac}(\omega) = \sigma_{dc} + A\omega^{s} \quad (6)$$

where σ_{dc} is dc conductivity, A is a frequency independent pre-exponential factor that depends only on temperature and s is the dimensionless frequency exponent having a value between 0 and 1; s is the degree of interaction between mobile ions with the environments surrounding them.

In order to identify the predominant conduction mechanism for $[(C_2H_5)_4N]FeCl_4$, different theoretical models proposed by Long *et al.* were used to correlate the conduction mechanism of AC conductivity with the predicted exponent $s(T)$ behavior.[34–37] These different models are: QMT, the quantum mechanical tunneling model, OLPT, the overlapping large polaron tunneling model, NSPT, the non-overlapping small polaron tunneling model, and CBH, the correlated barrier-hopping model. Comparing the obtained results with the extracted exponent s temperature dependence behavior (Fig. 9) for the different models, the conduction mechanism for $[(C_2H_5)_4N]FeCl_4$ was best interpreted with the correlated barrier hopping (CBH) model in region I and II.

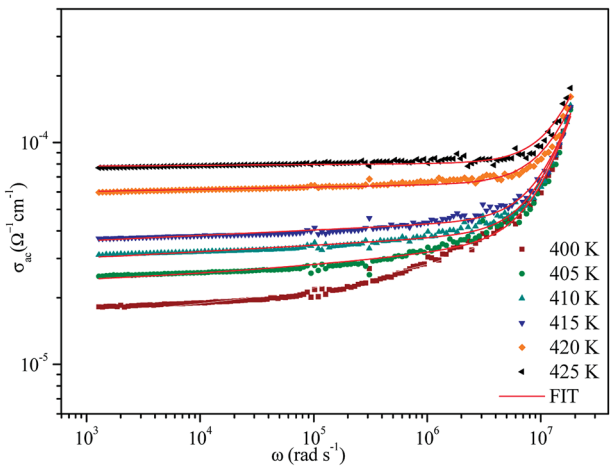

Fig. 8 Variation of σ_{ac} *versus* 1000/T at different frequencies.

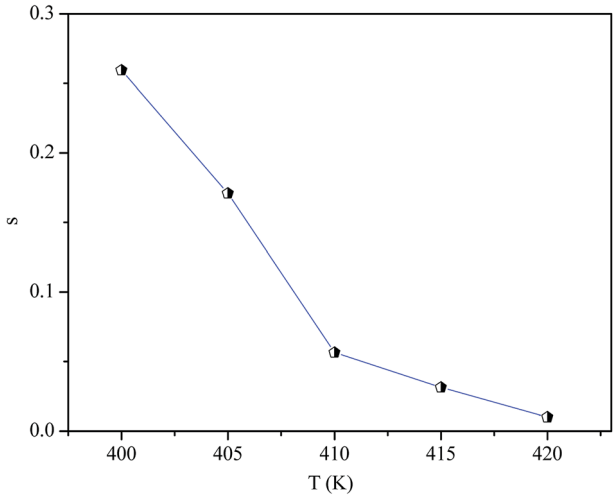

Fig. 9 Temperature dependence of the frequency exponent s.

According to this model of conduction[38] (CBH), the thermal dependence of S, is given by eqn (7):

$$s = 1 - \frac{6k_B T}{W_M - k_B T \ln(\omega\tau_0)} \quad (7)$$

where W_M is the polaron binding energy and τ_0 is the characteristic relaxation time. By a first approximation (at higher binding energy), eqn (8) is written in the form:

$$s = 1 - \frac{6kT}{W_M} \quad (8)$$

The AC conductivity as a function of frequency ($\sigma_{ac}(\omega)$) can be expressed according to this model[39,40] by eqn (9):

$$\sigma_{ac}(\omega) = \frac{n}{24}\pi^3 N^2 \varepsilon' \varepsilon_0 \omega R_\omega{}^6 \quad (9)$$

where n is the number of polarons participating in the hopping process ($n = 1$ for single polarons or 2 for bipolarons), N is the density of localized states in which carriers exist and R_ω is the hopping distance for the condition $\omega\tau = 1$ which is calculated using eqn (10):

$$R_\omega = \frac{e^2}{\pi\varepsilon_0\varepsilon'\left[W_M - k_B T \ln\left(\frac{1}{\omega\tau_0}\right)\right]} \quad (10)$$

The potential barrier W_M was calculated from the linear fit of the curve (1s) as a function of temperature from eqn (8). In the general case, if $W_M = E_a/2$, then bipolaron hopping is the dominating conduction mechanism and if $W_M = E_a/4$, then a single polaron is dominating. The obtained values of W_M are 0.12 eV in region I and 0.25 eV in region II. These values are proximate to $E_a/4$, which proves that single polaron hopping is the dominating conduction mechanism in the material. Temperature dependence of conductivity ($\ln(\sigma_{ac})$) at different frequencies is shown in Fig. 10. There is good agreement between experimental and theoretical curves. The density of localized states (N) obtained by fit are understood between 5.45

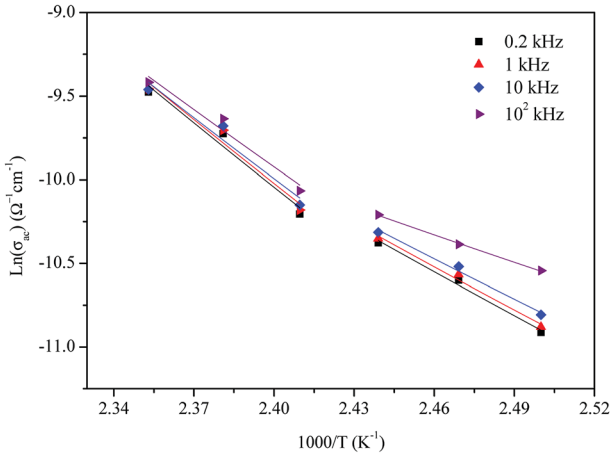

Fig. 10 Temperature dependence of $\ln(\sigma_{ac})$ at different frequencies.

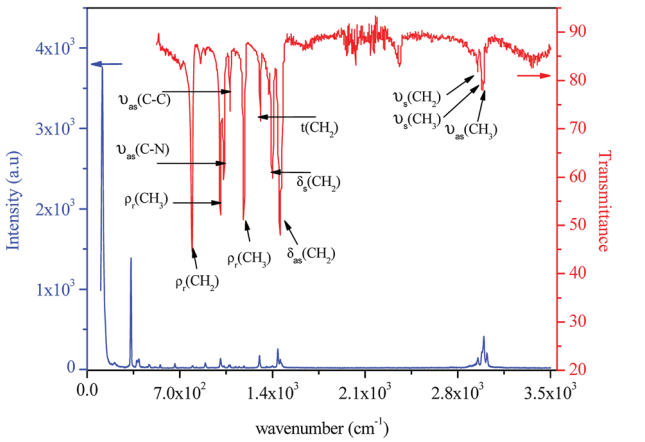

Fig. 11 Experimental IR and Raman spectra of $[(C_2H_5)_4N]FeCl_4$ at room temperature.

$\times 10^{34}$ to 5.12×10^{32} cm^{-1} in region I and between 3.02×10^{32} to 3.7×10^{31} cm^{-1} in region II. From a qualitative analysis of these values, we noted that the density of localized states decreased with increasing frequency. This reduction is explained by an increase in the disorder which decreased stabilities of states with non-localization of the latter.[41]

3.5 Vibrational study at room temperature

The IR and Raman spectra of tetraethylammonium tetrachloroferrate are presented in Fig. 11. Tentative assignments for a majority of the vibrational bands using previously reported data in the literature on similar compounds are: $[(C_2H_5)_4N]InBr_4$,[42] $[(C_2H_5)_4N]SbF_6$,[43] $[(C_2H_5)_4N]SbCl_6$,[44] $[(C_2H_5)_4N]_2CoCl_4$,[45] $[(C_2H_5)_4N]_2HgI_4$, $[(C_2H_5)_4N]Hg_3I_8$,[46] and $[(C_6H_5)_4P]FeCl_4$ (ref. 47) and are listed in Table 3.

Vibrations of the $[FeCl_4]^-$ anions. Symmetric and asymmetric bending vibrations ($\nu_2(FeCl_4)$ and $\nu_4(FeCl_4)$) are observed at 121 and 142 cm^{-1}, respectively. The strongest Raman band at 335 cm^{-1} is assigned to the symmetric stretching modes ($\nu_1(FeCl_4)$), whereas the asymmetric stretching vibration ($\nu_3(FeCl_4)$) gives the Raman peaks at 379 and 397 cm^{-1}.

The internal vibrations of the $[(C_2H_5)_4N]^+$ cations. The Raman spectrum above 3000 cm^{-1} displays one band (at *ca.* 3022 cm^{-1}) attributable to the (ν_{as} (CH_3)) vibration. The Raman and IR bands at 2990 and 2989 cm^{-1}, respectively, are attributed to the CH_2 asymmetric stretching mode ($\nu_{as}(CH_2)$). The IR peak at 2979 cm^{-1} is assigned to the CH_3 symmetric bending mode ($\delta_s(CH_3)$). On the other hand, the symmetric bending mode ($\delta_s(CH_2)$) is observed at 2952 and 2950 cm^{-1} in the Raman and IR spectra, respectively. The asymmetric bending of CH_2 groups ($\delta_{as}(CH_2)$) is found at 1460 and 1440 cm^{-1} in the Raman and at 1455 cm^{-1} in the IR spectra. The CH_3 symmetric bending ($\delta_s(CH_3)$) mode appears at 1353 cm^{-1} in the Raman spectrum. The observed Raman band at 1307 cm^{-1} and IR band at 1302 cm^{-1} are assigned to CH_2 twitching mode ($t(CH_2)$). The CH_3 rocking vibration ($\rho_r(CH_3)$) is in the Raman spectrum at 1185 and 1008 cm^{-1} and also as doublet IR bands at 1183 and 1006 cm^{-1}. The asymmetric stretching mode (ν_{as}(C–C)) is identified at 1082 cm^{-1} in Raman and at 1079 in IR, whereas the symmetric stretching mode (ν_s(C–C)) presents a Raman band at 895 cm^{-1}. The N–C asymmetric stretching vibration (ν_{as}(N–C)) is observed at 1022 and at 1033 cm^{-1} in Raman and IR, respectively, while the symmetric bending modes (ν_s(N–C)) are

Table 3 Observed Raman and IR frequencies in (cm^{-1}) of $[N(C_2H_5)_4]FeCl_4$[a]

$[(C_2H_5)_4N]FeCl_4$		
Raman (cm^{-1})	IR (cm^{-1})	Assignment
3022	—	$\nu_{as}(CH_3)$
2990	2989	$\nu_{as}(CH_2)$
—	2979	$\nu_s(CH_3)$
2952	2950	$\nu_s(CH_2)$
2937	—	
2890	—	
1460	1455	$\delta_{as}(CH_2)$
1441	—	
1400	1398	$\delta_s(CH_2)$
1353	—	$\delta_s(CH_3)$
1302	1307	$t(CH_2)$
1185	1183	$\rho_r(CH_3)$
1150	—	
1124	—	
1082	1079	ν_{as}(C–C)
1071	—	
1052	—	
1022	1033	ν_{as}(C–N)
1008	1006	$\rho_r(CH_3)$
895	—	ν_s(C–C)
794	791	$\rho_r(CH_2)$
665	—	ν_s(N–C)
554	—	δ_s(CNC)
516	—	
397	—	$\nu_3(FeCl_4)$
379	—	$\nu_3(FeCl_4)$
335	—	$\nu_1(FeCl_4)$
142	—	$\nu_4(FeCl_4)$
121	—	$\nu_2(FeCl_4)$

[a] ν_s, ν_1: Symmetric stretching; ν_{as}, ν_3: asymmetric stretching; δ_s, ν_2: symmetric bending; δ_{as}, ν_4: asymmetric bending; *t*: twitching; ρ_r: rocking.

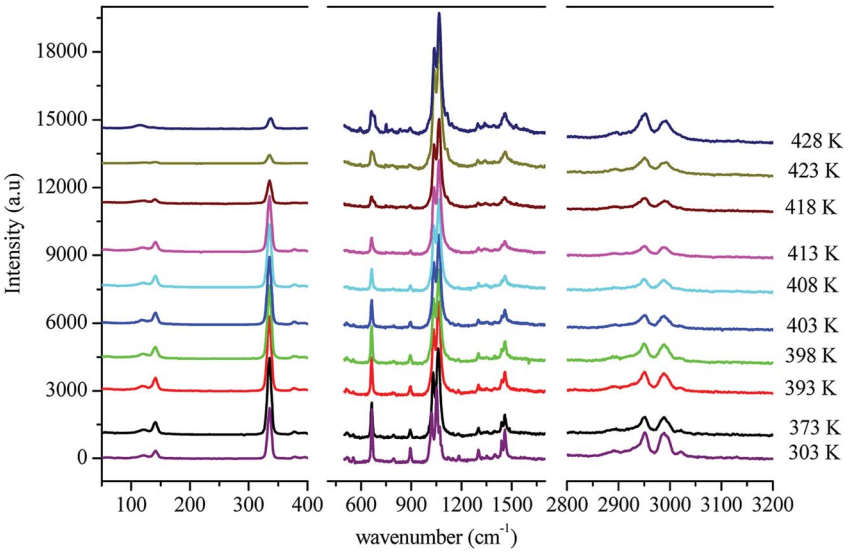

Fig. 12 Evolution of the Raman spectrum as a function of temperature.

located at 665 cm^{-1} in the Raman spectrum. A strong transmission band appearing in IR near 791 cm^{-1} and Raman band at 794 cm^{-1} are assigned to the CH_2 rocking vibration ($\rho_r(CH_2)$). The band related to the CNC skeleton deformation ($\delta_s(CNC)$) is detected in the Raman spectrum at 554 cm^{-1}.

3.6 Temperature dependence of the Raman spectra

In order to gain more information on the crystal dynamics and on the mechanism involved in the transition, we undertook a vibrational study using Raman scattering between 303 and 428 K.

Fig. 12 illustrates the Raman spectra of $[(C_2H_5)_4N]FeCl_4$ recorded in three spectral ranges ([50–400 cm^{-1}], [500–1600 cm^{-1}], and [2800–3200 cm^{-1}]). A deconvolution of all spectra was necessary to follow the temperature dependence of the wavenumber and half maximum. This deconvolution was carried out by means of Labspec software with a combination of two Lorentzian and Gaussian functions.

Fig. 14(a and b) shows the temperature dependence of the position and half maximum for some bands issued from the internal modes of the anionic part $[FeCl_4]^-$ observed between 50 and 400 cm^{-1}. We noticed that this figure indicates weak changes near 418 K where the phase transition has been observed. The line at 121 cm^{-1} associated with $\nu_2(FeCl_4)$ mode underwent a shift toward high frequency by 2 cm^{-1}, with a half maximum decrease by 5 cm^{-1}. The two bands at 379 and 397 cm^{-1} attributed to $\nu_3(FeCl_4)$ vanished at the temperature transition.

In Fig. 13(a and b), significant changes were obtained for some peaks located in the 500–1600 cm^{-1} frequency range which issued from the internal modes of the cationic parts. The two bands around 554 and 1185 cm^{-1} assigned to the $\delta_s(CNC)$ and $\rho_r(CH_3)$, respectively, vanished after the phase transition (418 K), while three bands appeared in the vicinity of 595, 750, and 1528 cm^{-1} at 418 K. A large change was detected for the peak at 665 cm^{-1} ($\nu_s(N–C)$), where it broke into two bands after 418 K. Another important change in the position was observed near 1440 and 1460 cm^{-1} ($\delta_{as}(CH_2)$). These two bands merged

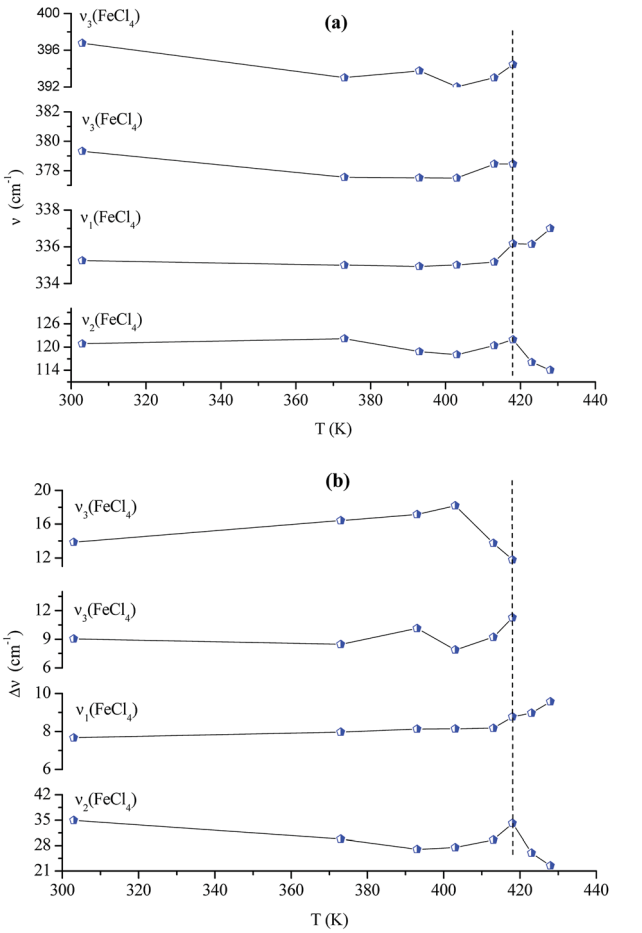

Fig. 13 Temperature dependence of some Raman position (a) and half-maximum (b) associated with the inorganic part.

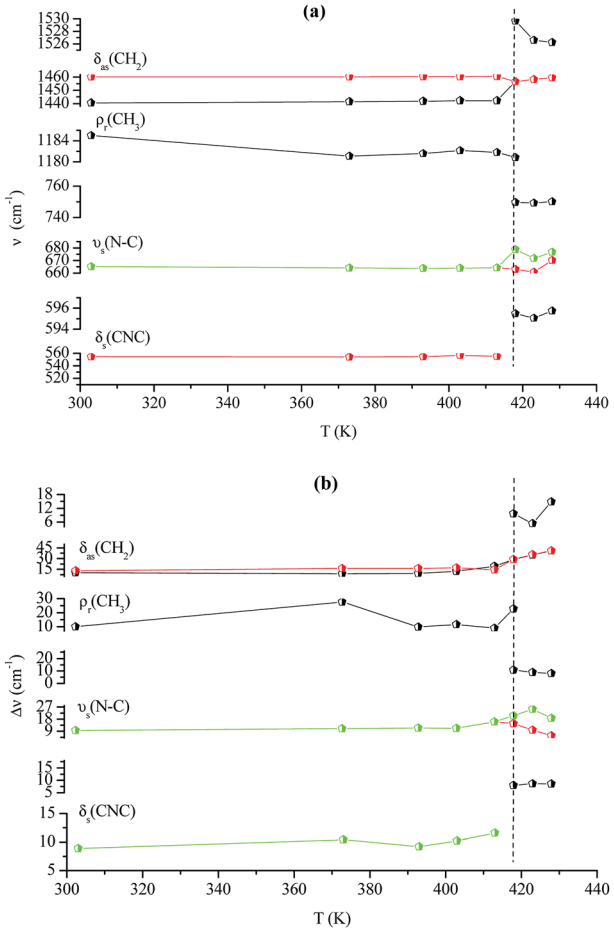

Fig. 14 Temperature dependence of some Raman position (a) and half-maximum (b) associated with the organic part.

into a single line at 418 K while the half maximum of them increased to 15 cm^{-1} above the transition. The bands observed between 2800 and 3200 cm^{-1}, which were assigned to the symmetric and asymmetric vibration of CH_2 and CH_3 groups, did not change significantly with temperature; their position and half maximum underwent weak changes (a few cm^{-1}) which means that these modes are not directly connected to a phase transition.

Spectral anomalies observed in Raman spectra of the $[(C_2H_5)_4N]FeCl_4$ crystals are due to a phase transition at $T = 418$ K which is in good agreement with DSC measurements and electrical proprieties. The most pronounced changes were found to be connected with vibration of the cationic part. In order to confirm the main role of the organic part in the phase transition point, we focused our study on the band around 1440 cm^{-1} associated with the CH_2 asymmetric bending mode $\delta_{as}(CH_2)$.

3.6.1 Temperature dependence of the Raman wavenumbers. According to Andrade and Porto,[48] the thermal dependence of the Raman shift of a phonon linked to an order–disorder mechanism can be expressed by eqn (11):

$$\nu^2 = \nu_0{}^2[1 + \gamma(T - T_t)] \quad (11)$$

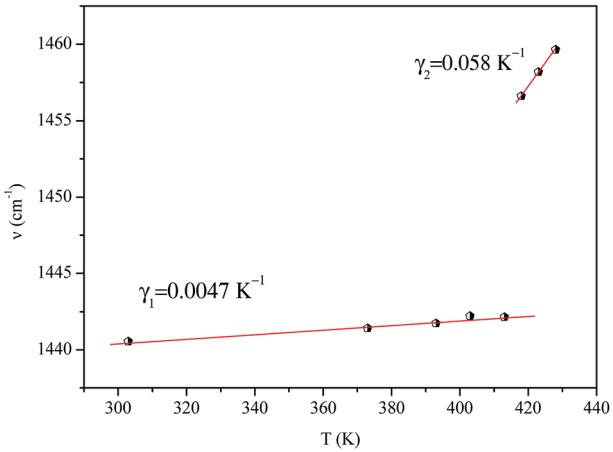

Fig. 15 Temperature dependence of the band position at 1440 cm^{-1}.

where ν_0 is the so-called 'hard-core wavenumber' at $T = T_{tr}$, γ is a thermal coefficient of the substance, and T_{tr} is the transition temperature. In the general case where γ is very weak, then eqn (11) can be written[49] as eqn (12):

$$\nu = \nu_0\left[1 + \frac{\gamma}{2}(T - T_t)\right] \quad (12)$$

The thermal coefficient γ associated with variation of the crystal volume and the wavenumber is given by eqn (13):

$$\gamma = -\frac{\Delta\nu}{\nu} \times \frac{V}{\Delta V} \quad (13)$$

where ν is the band position and V is the volume of the crystal at room temperature.

We adjusted the evolution of the frequency of the studied modes using eqn (12) in the temperature range that extends above and below the phase transition temperature (Fig. 15). The variation of the frequency shows two linear regimes, one below and the other above 418 K which confirms that this temperature is characterized by a phase transition. The value obtained from the coefficient (γ) at the level of the two temperature domains is in the order of 0.0047 K^{-1} for $T < T_{tr}$ and 0.058 K^{-1} for $T > T_{tr}$. We noticed that the parameter γ depends on the frequency and it increased with an increase in temperature, which makes it possible to identify that the volume of the crystal decreases for $T > T_{tr}$.[50]

3.6.2 Temperature dependence of the Raman at half maximum. The width of the Raman lines of a photon related to the order–disorder mechanism as a function of the correlation time (τ_c) can be obtained[51] from the generalized Langevin eqn (14):

$$\Gamma(\omega) = (a + bT) + c\frac{\tau_c}{1 + \omega^2\tau_c{}^2} \quad (14)$$

where τ_c is the correlation time (the time necessary to jump from one potential to another); it is related to orientational activation energy given by eqn (15):

$$\tau_c = \tau_0 \exp\left(\frac{E_a}{k_B T}\right) \quad (15)$$

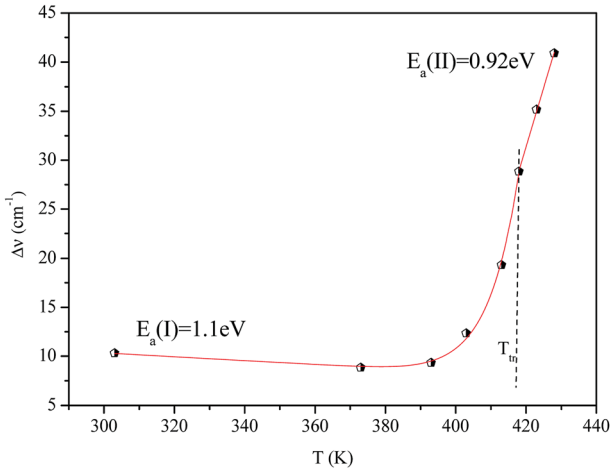

Fig. 16 Temperature dependence of the band half-widths at 1440 cm^{-1}.

where τ_0 represents the value of τ_c at high temperature, E_a is the activation energy for the concerned mode with the order–disorder transition, and k_B is the Boltzmann constant. Generally, the term $(\omega\tau_c^2) \gg 1$ so that eqn (14) can be reduced[52] to eqn (16):

$$\mathrm{FWWHM}(T) = (a + bT) + c\exp\left(-\frac{E_a}{k_B T}\right) \quad (16)$$

in which a, b, c, and E_a are parameters that should be fitted.

Fig. 16 shows the adjustment of the width at half maximum of the band at 1440 cm^{-1} using eqn (16). This variation is characterized by an enlargement at high temperature due to the reorientation dynamics of the disordered crystal. The activation energies determined from this spectrum are in the order of E_a (I) = 1.1 eV for $T < T_{tr}$ and E_a (II) = 0.92 eV for $T > T_{tr}$ which are in good agreement with the activation energies obtained by electrical conductivity.

The decrease of these values with increasing temperature is explained by the gradual evolution from an ordered state to a disordered phase resulting from an increase of the dynamics $[(C_2H_5)_4N]^+$ cation.[53] This allows us to conclude that the observed phase transition is related to the reorientation dynamical disorder of the tetraethylammonium cation.

4. Conclusion

Tetraethylammonium tetrachloroferrate with a hexagonal system ($P6_3mc$ space group) was prepared and investigated as a function of temperature and frequency. One phase transition at 413 K was detected by differential scanning calorimetry (DSC). Additionally, Nyquist plots revealed the existence of grains and grain boundaries that were fitted by an equivalent circuit. The AC conductivity spectrum was found to obey Jonscher's power law.

The temperature dependence of the exponents $s(T)$ indicated that a correlated barrier hopping (CBH) was the most suitable model for the conduction mechanism. Significant changes of several bands for the internal modes of the organic cation were observed within the phase transition temperature. Temperature dependence analysis of the frequency and the width of the $\delta_{as}(CH_2)$ mode proved that there is an anomaly around $T = 418$ K, a consequence of an order–disorder phase transition. The decrease of E_a values below the order–disorder phase transition can be understood as a change in the dynamical states of the cation.

Conflicts of interest

There are no conflicts to declare.

References

1 D. Braga, Crystal engineering, where from? where to?, *Chem. Commun.*, 2003, **22**, 2751–2754.
2 C. Sanchez, B. Julian, P. Belleville and M. Popall, Applications of hybrid organic–inorganic nanocomposites, *J. Mater. Chem.*, 2005, **15**, 3559–3592.
3 Y. Heng-Yun, T. Yuan-Yuan, L. Peng-Fei, L. Wei-Qiang, G. Ji-Xing, H. Xiu-Ni, C. Hu, S. Ping-Ping, Y. Yu-Meng and X. Ren-Gen, Metal-free three-dimensional perovskite ferroelectrics, *Science*, 2018, **361**, 151–155.
4 L. Wei-Qiang, T. Yuan-Yuan, L. Peng-Fei, Y. Yu-Meng and X. Ren-Gen, The Competitive Halogen Bond in the Molecular Ferroelectric with Large Piezoelectric Response, *J. Am. Chem. Soc.*, 2018, **140**, 3975–3982.
5 L. Wei-Qiang, T. Yuan-Yuan, L. Peng-Fei, Y. Yu-Meng and X. Ren-Gen, Large Piezoelectric Effect in a Lead-free Molecular Ferroelectric Thin Film, *J. Am. Chem. Soc.*, 2017, **139**, 18071–18078.
6 J. Binns, G. J. McIntyre, J. A. Barreda-Argueso, J. Gonzalez, F. Aguado, F. Rodriguez, R. Valiente and S. Parsons, Phase transition sequences in tetramethylammonium tetrachlorometallates by X-ray diffraction and spectroscopic measurements, *Acta Crystallogr., Sect. B: Struct. Sci., Cryst. Eng. Mater.*, 2017, **73**, 844–855.
7 A. R. Lim and K.-Y. Lim, Structural changes near phase transition temperatures for the $[N(C_2H_5)_4]$ groups in hydrated $[N(C_2H_5)_4]_2CuCl_4 \cdot xH_2O$, *J. Therm. Anal. Calorim.*, 2017, **130**, 879–884.
8 N. Moutia, M. Ben Gzaiel, A. Oueslati and K. Khirouni, Electrical characterization and vibrational spectroscopic investigations of order–disorder phase transitions in $[N(C_3H_7)_4]_2CoCl_4$ compound, *J. Mol. Struct.*, 2017, **1134**, 697–705.
9 A. Sen, S. Roy, S. C. Peter, A. Paul, U. V. Waghmare and S. Athinarayanan, Order–disorder structural phase transition and magnetocaloric effect in organic–inorganic halide hybrid $(C_2H_5NH_3)_2CoCl_4$, *J. Solid State Chem.*, 2018, **258**, 431–440.
10 C. Sanchez, B. Lebeau, F. Chaput and J. P. Boilot, Optical Properties of Functional Hybrid Organic–Inorganic Nanocomposites, *J. Adv. Mater.*, 2003, **15**, 1969–1994.
11 A. Oueslati, A. Bulou, F. Calvayrac, K. Adil, M. Gargouri and F. Hlel, Infrared, polarized Raman and *ab initio* calculations

of the vibrational spectra of $[N(C_3H_7)_4]_2Cu_2Cl_6$ crystals, *Vib. Spectrosc.*, 2013, **64**, 10–20.

12 M. Ben Gzaiel, A. Oueslati, I. Chaabane, A. Bulou, F. Hlel and M. Gargouri, Using Raman spectroscopy to understand the origin of the phase transitions observed in $[(C_3H_7)_4N]_2Zn_2Cl_6$ compound, *Spectrochim. Acta, Part A*, 2015, **145**, 223–234.

13 M. Gośniowska, Z. Ciunik, G. Bator, R. Jakubas and J. Baran, Structure and phase transitions in tetramethylammonium tetrabromoindate(III) and tetraethylammonium tetrabromoindate(III) crystals, *J. Mol. Struct.*, 2000, **555**, 243–255.

14 D. Wyrzykowski, R. Kruszynski, J. Kłak, J. Mrozinski and Z. Warnke, Magnetic Characteristics of Tetrabutylammonium Tetrahalogenoferrates(III): X-ray Crystal Structure of Tetrabutylammonium Tetrabromoferrate(III), *Z. Anorg. Allg. Chem.*, 2007, **633**, 2071–2076.

15 E. Coronado and P. Day, Magnetic Molecular Conductors, *Chem. Rev.*, 2004, **104**, 5419–5448.

16 D. Wyrzykowski, R. Kruszynski, J. Kłak, J. Mrozinski and Z. Warnke, Structural and magnetic characteristics of tetramethylammonium tetrahalogenoferrates(III), *Inorg. Chim. Acta*, 2008, **361**, 262–268.

17 J. a Puertolas, R. Navarro, F. Palacio and D. Gonzalez, Ferro and antiferromagnetic ordering in $N(C_2H_5)_4FeCl_4$ depending on the cooling rate, *J. Magn. Magn. Mater.*, 1983, **31**, 1067–1068.

18 Z. Warnke, E. Styczen, D. Wyrzykowski, A. Sikorski, J. Kłak and J. Mrozinski, Structural and physico-chemical characteristics of tetraethylammonium tetrachloridoferrate(III), *J. Struct. Chem.*, 2009, **21**, 285–289.

19 J. Rodriguez-Carvajal, Recent advances in magnetic structure determination by neutron powder diffraction, *Phys. B*, 1993, **192**, 55–69.

20 W. Trigui, A. Oueslati, I. Chaabane and F. Hlel, Synthesis, crystal structure, thermal analysis and dielectric properties of $[(C_4H_9)_4N]_3Bi_2Cl_9$ compound, *J. Solid State Chem.*, 2015, **227**, 10–16.

21 J. H. Joshi, D. K. Kanchan, M. J. Joshi, H. O. Jethvan and K. D. Parikh, Dielectric relaxation, complex impedance and modulus spectroscopic studies of mix phase rod like cobalt sulfide nanoparticles, *Mater. Res. Bull.*, 2017, **93**, 63–73.

22 N. Naveed, M. Mumtaz, R. Khan, A. A. Khan and M. Nasir khan, Conduction mechanism and impedance spectroscopy of $(MnFe_2O_4)_x$/CuTl-1223 nanoparticles-superconductor composites, *J. Alloys Compd.*, 2017, **712**, 696–703.

23 C. Yuan, X. Wu, J. Huang, X. Liu and B. Li, Electrical properties of thick film NTC thermistors based on $SrFe_{0.9}Sn_{0.1}O_{3-\delta}$, *Solid State Sci.*, 2010, **12**, 2113–2119.

24 P. Debye, *Polar molecules*, Dover, New York, 1929.

25 K. S. Cole and R. H. Cole, *J. Chem. Phys.*, 1941, **9**, 34.

26 D. W. Davidson and R. H. Cole, *J. Chem. Phys.*, 1951, **19**, 1484.

27 S. Havriliak and S. Negami, *J. Polym. Sci., Part C: Polym. Symp.*, 1966, **14**, 99.

28 T. Rhimi, M. Toumi, K. Khirouni and S. Guermazi, AC conductivity, electric modulus analysis of $KLi(H_2PO_4)_2$compound, *J. Alloys Compd.*, 2017, **714**, 546–552.

29 B. Banarji, P. Nayak and R. N. P. Choudhary, Impedance spectroscopy study of $NaBa_2V_5O_{15}$ ceramic, *J. Alloys Compd.*, 2007, **436**, 226–232.

30 P. S. Anantha and K. Hariharan, Structure and ionic transport studies of sodium borophosphate glassy system, *Mater. Chem. Phys.*, 2005, **89**, 428–437.

31 A. Elferjani, S. Garcia-Granda and M. Dammak, Synthesis, crystal structure, thermal analysis, dielectric properties and electrical conduction mechanisms of the new mixed solid solution of thallium rubidium sulfate selenate tellurate, *J. Alloys Compd.*, 2018, **749**, 448–464.

32 S. Hajlaoui, I. Chaabane, A. Oueslati and K. Guidara, Electrical transport properties and modulus behavior of the organic–inorganic $[N(C_3H_7)_4]_2SnCl_6$ compound, *Phys. B*, 2015, **474**, 90–96.

33 A. K. Jonscher, *Universal Relaxation Law*, Chelsea Dielectrics Press, London, 1996.

34 L. Zhang, J. Wang, F. Han, S. Mo, F. Long and Y. Gao, Crystal structure and electrical conduction of the new organic–inorganic compound $(CH_2)_2(NH_3)_2CdI_4$, *J. Mol. Struct.*, 2018, **1156**, 450–456.

35 A. Ghosh, Frequency-dependent conductivity in bismuth-vanadate glassy semiconductors, *Phys. Rev. B: Condens. Matter Mater. Phys.*, 1990, **41**, 1479–1488.

36 R. Long, Frequency-dependent loss in amorphous semiconductors, *J. Adv. Phys.*, 1982, **31**, 553–637.

37 S. R. Elliot, A.c. conduction in amorphous chalcogenide and pnictide semiconductors, *J. Adv. Phys.*, 1987, **36**, 135–217.

38 R. Megha, S. Kotresh, Y. T. Ravikiran, C. H. V. V. Ramana, S. C. Vijaya Kumari and S. Thomas, Study of alternating current conduction mechanism in polypyrrole-magnesium ferrite hybrid nanocomposite through correlated barrier hopping model, *Compos. Interfaces*, 2016, **24**, 55–68.

39 A. Zolanvari, N. Goyal and S. K. Tripathi, Electrical properties of a-Ge_xSe_{100-x}, *Pramana*, 2004, **63**, 617–625.

40 R. Ben Said, B. Louati and K. Guidara, Electrical properties and conduction mechanism in the sodium nickel diphosphate, *Ionics*, 2013, **20**, 703–711.

41 N. F. Mott and E. A. Davis, *Electronic Processes in Non-Crystalline Materials*, Clarendon Press, Oxford, 2nd edn, 1979.

42 M. Gośniowskaa, Z. Ciunika, G. Batora, R. Jakubasa and J. Bara, Structure and phase transitions in tetramethylammonium tetrabromoindate(III) and tetraethylammonium tetrabromoindate(III) crystals, *J. Mol. Struct.*, 2000, **555**, 243–255.

43 W. H. J. De Beer and A. M. Heyns, The I.R. and Raman spectra of tetraethylammonium hexafluoroantimonate $(C_2H_5)_4NSbF_6$, *Spectrochim. Acta, Part A*, 1981, **37**, 1099–1107.

44 T. Zeegers-Huyskens and G. Bator, Fourier transform infrared and Fourier transform Raman investigation of alkylammonium hexachloroantimonates, *Vib. Spectrosc.*, 1996, **13**, 41–49.

45 M. A. Kandhaswamy and V. Srinivasan, Synthesis and characterization of tetraethylammonium tetrachlorocobaltate crystals, *Bull. Mater. Sci.*, 2002, **25**, 41–45.

46 A. Hooper and D. W. James, Vibrational spectra of crystalline halomercurate(II) complexes, *Aust. J. Chem.*, 1971, **24**, 1331–1344.

47 G. P. Bhavsar and K. Sathianandan, Vibrational analysis of tetrahaloferrates of the type $FeCl_{4-n}Br_{-1n}$, *J. Mol. Struct.*, 1973, **6**, 343–345.

48 P. d. R. Andradet and S. P. S. Porto, Hard core phonon frequency at transition temperature, *Solid State Commun.*, 1974, **14**, 547–550.

49 V. Venkataramanan and M. R. Srinivasan, Vibrational spectroscopic study of zinc tris(thiourea) sulphate, a new organometallic non-linear optical crystal, *J. Raman Spectrosc.*, 1994, **25**, 805–811.

50 M. Oussaid, P. Becker and C. C. Nedelec, Raman scattering investigation of order–disorder phase transitions in cadmium tris(thiourea) sulphate (CTS), *J. Raman Spectrosc.*, 2000, **31**, 529–533.

51 A. M. Amorim da Costa, A. M. Amado, M. Becucci and C. Kryschi, Order–disorder phase transition in *p*-terphenyl and *p*-terphenyl: tetracene doped crystals as studied by Raman spectroscopy, *J. Mol. Struct.*, 1997, **416**, 69–73.

52 G. Bator, R. Jakubas and J. Baran, Vibrational study of the structural phase transitions in the $(CH_3ND_3)_3Sb_2Br_9$ (d-MABA) crystals by infrared spectroscopy, *Vib. Spectrosc.*, 2001, **25**, 101–113.

53 N. Weslati, I. Chaabane and F. Hlel, Raman investigation of the order–disorder phase transitions in the $2[N(C_3H_7)_4]SbCl_4$ compound, *Vib. Spectrosc.*, 2015, **81**, 90–95.

